Effects of structure, composition, and carbon support properties on the electrocatalytic activity of Pt-Ni-graphene nanocatalysts for the methanol oxidation

Yaojuan Hu, Ping Wu, Yajing Yin, Hui Zhang, Chenxin Cai*

Jiangsu Key Laboratory of New Power Batteries, Jiangsu Key Laboratory of Biofunctional Materials, Laboratory of Electrochemistry, College of Chemistry and Materials Science, Nanjing Normal University, Nanjing 210097, PR China

ARTICLE INFO

ABSTRACT

The structure, composition, morphology, and support material significantly affect the catalytic characteristics of Pt-based nanocatalysts. Fine control of the structural and compositional features is highly favorable for the creation of new Pt-based nanocatalysts with enhanced catalytic performance and improved Pt utilization. This work reports on a systematic and comparative study of the effects of structure, composition, and carbon support properties on the electrocatalytic activity and stability of Pt-Ni bimetallic catalysts for methanol oxidation, particularly the promoting effect of Ni on Pt. Graphene-supported Pt-Ni alloy nanocatalysts were prepared by a facile, one-step chemical reduction of graphene oxide and the precursors of Ni^{2+} and $PtCl_6^{2-}$. The nanocatalysts were characterized by transmission electron microscopy (TEM), ultraviolet–visible spectrophotometry (UV–vis), X-ray photoelectron spectroscopy (XPS), energy-dispersive X-ray spectroscopy (EDS), and X-ray diffraction (XRD). The electrocatalytic characteristics of the nanocatalysts were studied by voltammetry with methanol oxidation as a model reaction to evaluate the effects of the structure, surface composition, and electronic characteristics of the catalyst on the electrochemical activity. The catalyst with a Pt/Ni molar ratio of 1:1 exhibited the highest electrocatalytic activity for the methanol oxidation reaction with greatly lowered Pt utilization. The mechanism of the promoting effect of Ni on Pt is explained based on the modification of the electronic characteristics of the surface Pt atoms (Pt 4f) by Ni atoms due to the shift in the electron transfer from Ni to Pt and the synergistic roles of Pt and nickel hydroxides on the surfaces of the catalysts. The effects of the different carbon supports (i.e., graphene, single-walled carbon nanotubes, and Vulcan XC-72 carbon) on the electrocatalytic characteristics of the nanocatalysts are investigated by Raman and XPS experiments. The results demonstrate that the graphene-supported Pt-Ni catalyst has the highest electrocatalytic activity of the three carbon materials due to abundant oxygen-containing groups on the graphene surface, which can remove the poisoned intermediates and improve the electrocatalytic activity of the catalysts.

1. Introduction

Future energy concerns demand a transition from fossil fuels to new energy sources that are more environmentally benign and renewable. A promising route for accomplishing this goal is to use fuel cells to convert the chemical energy of fuel directly into electricity. In this sense, direct methanol fuel cells (DMFCs) have received much attention because of several advantages, including high conversion efficiency, low pollution, light weight, ease in liquid handling, low operating temperature, and high power density, for a wide range of applications (e.g., power sources in automobiles,

space shuttles, buildings, and factories) [1–3]. The main reactions occurring within DMFCs are the cathodic oxygen reduction reaction (ORR) and the anodic methanol oxidation reaction (MOR). The Pt catalyst is one of the best catalysts for ORR and MOR, and it is a key component in DMFCs in terms of its activity and its stability. The Pt catalyst accounts for approximately 30% of the cost to manufacture the fuel cells. The catalytic characteristics of the catalysts are strongly dependent on their size, shape, and morphology [4–10]. Fine control of the structural features is highly favorable for the creation of new Pt nanocatalysts with enhanced catalytic performance and improved Pt utilization. To enhance the electrocatalytic activity, much effort has been devoted to preparing various forms of Pt catalysts, such as mesoporous Pt [11], highly ordered Pt nanotube arrays [12], and three-dimensional dendritic Pt nanostructures [13]. However, pure Pt catalysts are readily

* Corresponding author.
E-mail address: cxcai@njnu.edu.cn (C. Cai).

poisoned at low temperatures by CO, which is a byproduct of methanol electrooxidation [14–16].

One method that has been demonstrated to improve the catalytic activity and to lower the cost of the catalysts is the alloying of platinum with other transition metals, on the basis of a bifunctional mechanism, an electronic effect, or an ensemble effect [17–26]. The Pt-based binary and ternary metallic catalysts (e.g., Pt-Fe, Pt-Ni, Pt-Cr, Pt-Cu, Pt-Au, Pt-CO, and Pt-Fe-Co) have been studied in terms of the ORR to enhance the catalytic activity, to improve the stability, and to reduce the use of Pt [17,18,20,21,23,27–32]. The enhanced catalytic activities have been attributed to a number of factors, including lattice shrinking or lattice strain due to changes in the Pt–Pt bond distance, D-band center shift, and a Pt skin effect [17]. However, the alloy catalysts of Pt-transition metal have not widely studied for MOR [16,19,22]. The addition of Ni to Pt or to PtRu catalysts was recently shown to improve the activity of these catalysts toward MOR in acid and alkaline media [2,33–35]. The promoting mechanism of Ni on Pt in the Pt-Ni catalyst is not fully understood. The precise role played by the composition on the modification of the electronic characteristics of Pt by Ni in the enhancement of the catalytic activity remains unclear. This work is a systematic and comparative study of the effects of the structure, composition, and the carbon support properties on the electrochemical activity and stability of the Pt-Ni bimetallic catalyst for MOR, particularly the promoting effect of Ni on Pt.

Several factors affect the catalyst performance, such as the preparation method, the supporting materials, and the pretreatment of the materials [36–38]. The supporting material is a crucial factor in determining the particle size and distribution of the metal nanoparticles located on its surface, and it simultaneously has a significant influence on the catalytic performance, utilization, and stability of the supported catalyst [39–41]. For practical considerations, loading the catalysts onto the surface of suitable supporting materials to enhance their activity and to decrease the use of Pt is highly desired. An ideal supporting material should have high inertness in harsh chemical and electrochemical conditions, a large surface area for good dispersion of the catalyst nanoparticles, high electrical conductivity, and low cost [37,42]. Many carbon materials have been investigated as catalyst supports for DMFCs, such as Vulcan XC-72 carbon [43,44], carbon nanotubes (CNTs) [45], carbon nanofibers [46], and mesoporous carbon [19,47,48]. Vulcan XC-72 carbon is a popular support for catalysts; however, it has poor corrosion tolerance in the working conditions of DMFCs [41]. For CNTs as catalyst supports, the simple deposition of the catalyst onto pristine CNTs leads to poor dispersion and instability [49]. Modifying the CNTs surface with desired functional groups by different treatment methods is a common strategy to obtain well-dispersed metal nanoparticles on CNTs, but these treatments can damage the integrity and intrinsic conductivity of the tubes, lowering the overall electrocatalytic activity and stability [19]. Therefore, finding a novel carbon material as a support to achieve lower loading of platinum with high catalytic performance and increased utilization of the catalyst is important.

Graphene, which is the basic structure of all graphitic forms, has drawn much attention because of its unusual electronic properties and ability to improve catalytic properties [50–52]. The surface of graphene contains abundant oxygen functional groups [53,54] that can efficiently disperse metal nanoparticles and can remove accumulated carbonaceous species (e.g., CO), resulting in higher electrocatalytic activity by the catalyst [55–57]. Therefore, graphene can be a potential application as a catalyst support [58–62]. This work compares Vulcan XC-72 carbon, single-walled carbon nanotubes (SWNTs), and graphene as supporting materials to prepare Pt-Ni catalysts for the oxidation of methanol. The catalysts supported on the different carbon materials were fabricated by a facile, one-step chemical reduction method and

were characterized by transmission electron microscope (TEM), ultraviolet–visible spectrophotometry (UV–vis), X-ray photoelectron spectroscopy (XPS), energy-dispersive X-ray spectroscopy (EDS), and X-ray diffraction (XRD). The electrocatalytic characteristics of the nanocatalysts for MOR were investigated by voltammetry and chronoamperometric measurements. The results show that the graphene-supported Pt-Ni catalyst has the highest electrocatalytic activity toward the MOR among the three carbon materials. The mechanism of the effects of the different carbon supports on the electrocatalytic performance of the catalyst is explained with the results from the Raman and XPS experiments.

2. Experimental

2.1. Chemicals

Graphite powder (99.998%, 325 mesh, Alfa Aesar), $H_2PtCl_6·6H_2O$ (Sinopharm Chemical Reagent Co. Ltd.), $NiCl_2·6H_2O$ (Shanghai Chemical Reagent Co. Ltd., Shanghai, China), hydrazine (Shanghai Chemical Reagent Co. Ltd.), poly(vinyl pyrrolidone) (PVP, $M_W ≈ 10,000$, Aldrich), and Vulcan XC-72 carbon (Cabot) were used as received. Single-walled carbon nanotubes (<2 nm in diameter) were obtained from Shenzhen Nanotech Port (Shenzhen, China). Prior to use, the SWNTs were sonicated in a 1:3 mixture of concentrated HNO_3 and H_2SO_4 for 2 h. The SWNTs were then washed thoroughly with double-distilled water, centrifuged, and dried under vacuum at ambient temperature. The Fourier transform infrared (FTIR) spectroscopic results indicated that oxygen-containing functional groups were generated on the walls of the SWNTs after treatment.

2.2. Synthesis of graphene oxide (GO) sheets

GO was prepared by a modified Hummer's method [63], which involves graphite oxidation and exfoliation. Graphite powder (3 g) was put into a mixture of concentrated H_2SO_4 (12 mL), $K_2S_2O_8$ (2.5 g), and P_2O_5 (2.5 g). The solution was heated to 80 °C in an oil bath and stirred for 4.5 h. Next, the mixture was cooled to room temperature and diluted with double-distilled water (0.5 L) and left overnight. Then, the product was obtained by filtering through a 0.2 μm Nylon film and washed with double-distilled water to remove the residual acid. The product was dried at ambient temperature.

The pretreated graphite powder was put into cold (0 °C), concentrated H_2SO_4 (120 mL). Then, $KMnO_4$ (15 g) was added gradually while stirring, and the temperature of the mixture was kept below 20 °C using an ice bath. Successively, the mixture was stirred at 35 °C for 2 h and then diluted with double-distilled water (0.5 L) to keep the temperature at 50 °C. After adding 250 mL of double-distilled water, the mixture was stirred for 2 h, and then additional water (1 L) was added. Shortly after the dilution, 30% H_2O_2 (20 mL) was added drop by drop, and the color of the mixture changed to a brilliant yellow while bubbling. The mixture was filtered and washed with a 1:10 HCl aqueous solution (1 L) to remove metal ions, which was followed by a double-distilled water wash (1 L) to remove the acid. The resulting solid was dried in air and diluted to make a graphite oxide dispersion (0.5% w/w). Finally, the mixture was purified by performing dialysis for one week to remove the remaining metal species.

Exfoliation was carried out by sonicating the graphite oxide dispersion (1 mg mL^{-1}) under ambient conditions for 30 min. The resulting homogeneous yellow–brown dispersion was then subjected to 30 min of centrifugation at 3000 rpm to remove unexfoliated graphite oxide (usually present in a very small amount). Atomic force microscopy (AFM) images recorded with a Nanoscope

IIIa scanning probe microscope (Digital Instruments) using the tapping mode indicated that the thickness of the prepared GO was approximately 1 nm (the AFM image is not shown here), which agrees with the reported apparent thickness of GO sheets [53] and suggests that the single-sheet nature of GO is obtained. The AFM images revealed that no sheets either thicker or thinner than 1 nm are observed, demonstrating that complete exfoliation of GO down to an individual sheet is achieved under our experimental conditions.

2.3. Preparation and characterization of the catalysts

The graphene-supported Pt-Ni alloy nanocatalysts (denoted as Pt-Ni-graphene) were prepared via a one-step chemical reduction (hydrazine reduction) method. The process is described as follows. The required amounts of $H_2PtCl_6 \cdot 6H_2O$ and $NiCl_2 \cdot 6H_2O$ were dissolved in 50 mL of the GO suspension (1 mg mL^{-1}, suspended in water). Then, 0.2 g PVP was added into the mixed solutions. PVP is a linear polymer and is one of the common functional capping agents in the synthesis of metal or metal alloy nanomaterials [64]. The role of PVP is to stabilize the Pt or Pt-Ni nanocatalysts via bonding the pyrrolidone ring with the surface of the catalysts, and to improve the dispersion of nanocatalysts, and therefore prevent the nanoparticles from random aggregation. Subsequently, 40 μL of hydrazine and 400 μL of NaOH (1 M) were successively added into the reaction mixture. The pH value of the reaction system was adjusted with NaOH to be approximately 10.5. The mixed solution was magnetically stirred for 12 h at ambient temperature. During this process, GO was reduced to graphene, and the precursors of $PtCl_6^{2-}$ and Ni^{2+} ions were reduced to Pt-Ni alloy particles and deposited onto the surface of graphene, resulting in Pt-Ni-graphene nanocatalysts. The nanocatalysts were collected by centrifugation, washed sequentially with double-distilled water several times until no Cl$^-$ ions were detected, and dried overnight in vacuum at ambient temperature. The Cl$^-$ ions were detected using $AgNO_3$ solution. If no white precipitate appeared after $AgNO_3$ solution was added into the centrifugate, it can be assumed that no Cl$^-$ ions were presented in it. By adjusting the amount of the metal precursors, Pt-Ni-graphene nanocatalysts with Pt/Ni ratios of 1:0.5, 1:1, and 1:2 were prepared. The total metal (Pt + Ni) loading of the nanocatalysts was controlled to be approximately 40 wt%. A similar process was used to prepare 40 wt% Pt-graphene nanocatalysts.

The Pt-Ni nanocatalysts with Pt/Ni molar ratios of 1:1 and metal loading of 40 wt% were also prepared on SWNTs (Pt-Ni-SWNT) and Vulcan XC-72 carbon (Pt-Ni-XC-72C) using a similar procedures as described above to study the role of graphene in improving the electrocatalytic activity of the Pt-Ni-graphene nanocatalysts.

The crystalline structures of the prepared nanocatalysts were examined by X-ray diffraction (XRD, Rigaku/Max-3A X-ray diffractometer) with Cu Kα radiation (λ = 0.15418 nm). The size distribution and the mean sizes of the nanocatalysts were determined by a BI-200SM dynamic light scattering (DLS) instrument (Brookhaven Instruments). The particle shape and the degree of dispersion of the nanocatalysts on the surfaces of the supporting materials were confirmed by transmission electron microscopy and high-resolution TEM (HRTEM), which were carried out on a JEOL-2010 transmission electron microscope operating at an accelerating voltage of 120 kV. The samples were prepared by dispersing the nanocatalysts in ethanol and evaporating one drop of the suspension onto a carbon-coated film supported on a copper grid for TEM measurements. The loading and the composition of the prepared Pt-Ni nanocatalyst on the graphene were analyzed by an inductively coupled plasma-atomic emission spectroscopy (ICP-AES, Prodigy, Teledyne Leeman Labs) and energy-dispersive spectroscopy. The EDS data were recorded with an Oxford Link ISIS energy-dispersive spectrometer fixed on the microscope. The

surface characteristics of the nanocatalysts were examined by X-ray photoelectron spectroscopy, which were recorded on an ESCALAB 250 XPS spectrometer (VG Scientifics) using the monochromatic Al Kα line at 1486.6 eV. The binding energies were calibrated with respect to the C (1s) peak at 284.6 eV. The peak fit analysis was performed using the XPS PEAK program (version 4.0). The UV–vis spectra were recorded using a Cary 5000 UV–vis–NIR spectrophotometer (Varian), and the Raman spectra were recorded with a Labram HR800 UV (Jobin Yvon) Raman spectrometer at ambient temperature using an excitation wavelength of 514.5 nm and a spectral slit width of 2 cm^{-1}.

2.4. Electrochemical measurements

The electrochemical measurements were performed with a CHI 660B electrochemical workstation (CH Instruments). A conventional three-electrode system was used with a glassy carbon (GC) electrode (3 mm in diameter) as a working electrode. A coiled Pt wire and a saturated calomel electrode (SCE) were used as the counter electrode and the reference electrode, respectively. Prior to use, the GC electrode was polished sequentially with alumina grain sizes of 0.3 μm and 0.05 μm to create a mirror finish. The electrode was then sonicated with absolute ethanol and double-distilled water for approximately 1 min, and it was rinsed thoroughly with double-distilled water and dried under ambient temperature. A 6-μL suspension of Pt-Ni-graphene nanocatalysts (2 mg mL^{-1}), which was prepared by sonicating the nanocatalysts in water for 30 s, was cast onto the surface of the pretreated GC electrode with a microsyringe, and the solvent was allowed to evaporate at ambient temperature before use. An aqueous solution of 0.5 M H_2SO_4 was used as the electrolyte. For MOR, the electrolyte solution was purged with high-purity nitrogen for at least 30 min prior to each electrochemical measurement, and a nitrogen environment was maintained over the solution to prevent the solution from oxygen. The electrocatalytic currents were normalized with the mass of platinum loading on the electrode surface. The catalytic stability of the catalyst was evaluated with amperometric measurements under an applied potential of 0.64 V.

The electrocatalytic characteristics of the Pt-Ni-SWNT and Pt-Ni-XC-72C nanocatalysts (with Pt/Ni molar ratios of 1:1) were also studied for the MOR. The electrochemical measurements were performed at ambient temperature (22 ± 1 °C).

3. Results and discussion

3.1. Preparation and characterization of the graphene-supported Pt-Ni nanocatalysts

The Pt-Ni-graphene nanocatalysts were prepared by a facile one-step reduction of GO and the precursors of Ni^{2+} and $PtCl_6^{2-}$ ions. Hydrazine was chosen as the reduction agent because it can lead to formation of the Pt-Ni nanocatalyst with a high degree of alloying and low oxide content. To minimize the large gap in redox priority between Pt and Ni, an aqueous solution reaction system was chosen because the water molecules in the reaction system can promote reduction [21]. The reduction processes were characterized according to the UV–vis spectra (Fig. 1). The UV–vis spectrum of GO (1 mg mL^{-1}) in water shows a maximum absorption peak at approximately 230 nm (curve a), corresponding to the $\pi \rightarrow \pi^*$ transition of aromatic C–C bonds [65], which agrees with previous reports [66,67]. The absorption peaks of Ni^{2+} (1 mM) and $PtCl_6^{2-}$ (1 mM) ions appear at 390 nm [68] (curve b) and 259 nm [69] (curve c), respectively. Mixing the precursors of Ni^{2+} (1 mM) and $PtCl_6^{2-}$ (1 mM) does not alter the UV–vis absorption features of the Ni^{2+} and $PtCl_6^{2-}$ ions (curve d). After reduction with hydrazine, the
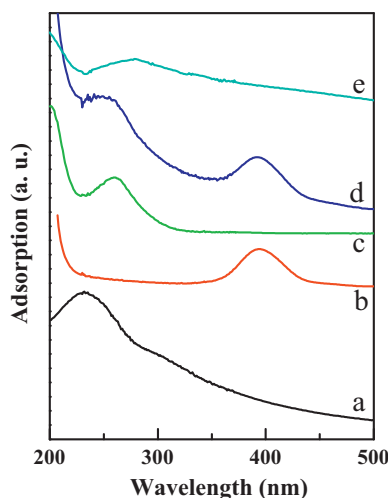
Fig. 1. UV–vis spectra of GO ((a) 1 mg mL^{-1}), NiCl$_2$ ((b) 1 mM), H$_2$PtCl$_6$ ((c) 1 mM), the mixture of NiCl$_2$ (1 mM) and H$_2$PtCl$_6$ (1 mM) (d), and the Pt-Ni-graphene (e) in aqueous solutions.

peak corresponding to the absorption of GO, Ni^{2+} ions, and PtCl$_6$$^{2-}$ ions disappears, and a broad absorption peak is observed at 270 nm (curve e), which is the characteristic electronic conjugation within the graphene sheets [66,67]. These results demonstrate that the simultaneous reduction of GO, Ni^{2+} ions, and PtCl$_6$$^{2-}$ ions and the formation of the graphene-supported bimetallic Pt-Ni nanocatalysts.

The simultaneous reduction of GO, Ni^{2+} ions, and PtCl$_6$$^{2-}$ ions by hydrazine was also verified by XPS measurements. Fig. 2 shows the XPS spectra of the GO (curve a) and Pt-Ni-graphene nanocatalysts (curve b). A typical XPS spectrum of GO shows a C1s peak at 284.6 eV and a O1s peak at 532.7 eV with a carbon/oxygen (C/O) atomic ratio of approximately 1.8 (curve a), which was estimated by integrating the peak area in the XPS spectra after the background correction. After reduction by hydrazine, the peak of O1s decreased significantly (curve b) in comparison with that shown in curve (a), and the C/O ratio increased to approximately 8.3, which is much higher than GO, suggesting the reduction of GO to graphene. In addition, the Pt4f (ca. 72.2 eV), Ni2p (ca. 857.3 eV), and N1s peaks (ca. 399.8 eV) are observed in the XPS spectrum of Pt-Ni-graphene nanocatalysts (curve b). No XPS peaks of Cl$^-$ ions can be observed, suggesting that the Cl$^-$ ions were completely removed during washing. The N1s peak is ascribed to the doping of N atoms in the reduction of GO in the presence of hydrazine [70]. The positions of Pt4f and Ni2p agree
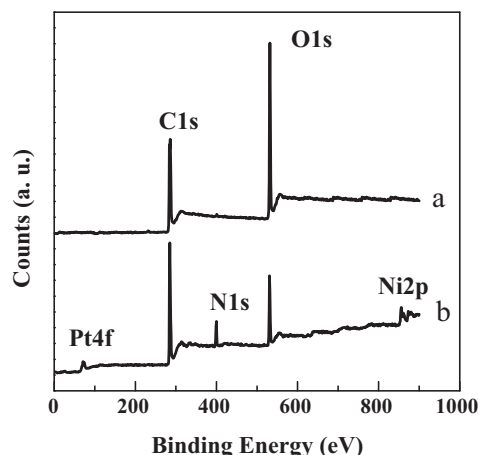
with those reported for Pt-Ni alloy [24,71], indicative of the reduction of these precursors and the formation of the Pt-Ni-graphene nanocatalysts.

Due to its low redox potential as compared to Pt, Ni loss may occur during the reduction of Ni^{2+} and PtCl$_6$$^{2-}$ ion by hydrazine. Therefore, the metal loading on the graphene for the prepared nanocatalysts was analyzed and confirmed by ICP-AES measurements. Forty weight percent of the total metal loading can be achieved. This value is the same as the precursors involved in the reaction mixtures, indicative of the complete reduction of the Ni precursor in our experimental conditions. The compositions of individual particle of the nanocatalysts were estimated by EDS. The EDS results for the Pt-Ni catalysts revealed the presence of C, N, Pt, and Ni, and no other element was detectable, suggesting that the nanocatalysts deposited on the graphene surface were Pt-Ni nanoparticles (the EDS spectra are not shown here). The atomic ratios between Pt and Ni in individual particle of the prepared nanocatalysts were very close to the nominal values as indicated by the data in Table 1, demonstrating that the molar ratios of Pt/Ni in individual particle of the prepared nanocatalysts were almost the same as the precursors involved in the reaction mixtures.

The graphene-supported Pt-Ni nanocatalysts with different Pt/Ni molar ratios were characterized by TEM and HRTEM. The GO sheets are rippled and resemble crumpled silk veil waves (Fig. 3a). The TEM images show remarkably uniform Pt-Ni nanocatalysts that are well dispersed on the graphene surface (Fig. 3b–e). All of the nanoparticles were considered to be spherical with a mean particle diameter of approximately 34–38 nm, as evaluated by DLS analysis (the insets in Fig. 3b–e), regardless of the molar ratios of Pt/Ni. Because the particle size was nearly identical for the nanocatalysts prepared at different Pt/Ni molar ratios, the effects of the particle size on their catalytic activities could be neglected.

The HRTEM image of the Pt-Ni-graphene nanocatalyst recorded for the Pt/Ni molar ratio of 1:1 shows the dominant formation of the face-centered cubic (fcc) (1 1 1) lattice image (Fig. 3f). The lattice spacing is observed to be 0.223 nm, which agrees with the d-spacing calculation from the XRD pattern (Table 1; discussed below). However, this value is slightly smaller than that of the (1 1 1) plane of Pt (0.23 nm [72]) due to the contraction of the lattice upon substitution of a Pt atom with a Ni atom.

The crystalline structures of the Pt-Ni-graphene nanocatalysts were confirmed by XRD measurements (Fig. 4). The diffraction peak located at approximately 25.1° is associated with the carbon (0 0 2) from graphene [73], as shown in curve a (Fig. 4). For Pt-graphene, the peaks at approximately 39.8°, 46.4°, 67.6°, and 81.8° are characteristic of fcc crystalline Pt (curve b), corresponding to the planes (1 1 1), (2 0 0), (2 2 0), and (3 1 1) (JCPDS 04-0802), respectively, and are indicative of the formation of fcc-structured Pt on graphene. For the Pt-Ni-graphene nanocatalysts, the XRD patterns demonstrate the characteristic peaks of the Pt fcc structure. No characteristic peaks of Ni or its oxides are detected (curves c–d), indicative of the formation of alloys of Pt and Ni. In addition, the corresponding peaks shift slightly to higher angles as compared to those of Pt-graphene, thereby indicating a contraction of the lattice upon substitution of Pt with Ni. This finding is supported by the fact that Ni atoms are 11% smaller relative to Pt atoms [21] and that the substitution within a solid solution usually occurs when the size of the smaller atom is at least 87% of the larger one. Moreover, this result agrees with the HRTEM analysis.

The d-spacing values and the lattice parameter (a) of Pt in the Pt-Ni nanocatalysts at different molar ratios were calculated and are shown in Table 1. The d-spacing values and the lattice parameter of Pt in the Pt-Ni nanocatalysts are smaller than those in Pt-graphene, and they decrease further with increases in the molar ratio of Ni in the Pt-Ni catalysts. These results suggest the replacement of Pt atoms by Ni atoms, which is further evidence of the formation of

Fig. 2. The XPS spectra of the GO (a) and Pt-Ni-graphene nanocatalysts (b).

Table 1
A summary of the atomic ratios of Pt to Ni, the d-spacing values (d), and the lattice parameter (a) of the Pt-Ni-graphene nanocatalysts.

Nominal atomic ratio of Pt to Ni	Actual atomic ratio of Pt to Ni[a]	2θ for Pt (1 1 1) (°)	d-spacing (nm)[b]	Lattice parameter (nm)[c]
Pure Pt		39.8	0.2264	0.3921
1:0.5	1:0.48	40.1	0.2246	0.3890
1:1	1:0.96	40.4	0.2234	0.3869
1:2	1:2.04	30.6	0.2224	0.3852

[a] Estimated by the EDS measurements.

[b] The value of d was calculated using Bragg's equation: $2d\sin\theta = n\lambda$.

[c] The value of a was calculated using the equation $d_{h\,k\,l} = a/\sqrt{h^2 + k^2 + l^2}$ for the face centered-cubic crystal system.

Pt-Ni alloys [74]. By carefully analyzing the dependence of the value of the lattice parameter on the compositions of the Pt-Ni catalysts, the lattice parameters of the catalysts are linearly dependent on the composition (not shown here), as predicted by Vegard's law (a linear decrease of the lattice constant occurs with an increase in the amount of Ni substituted into the Pt matrix because both Pt and Ni are fcc structures) [21]. This result also supports the formation of the Pt-Ni alloy.

The XRD and HRTEM results indicate that the geometric environment of the Pt atoms in Pt-Ni alloys is changed due to the
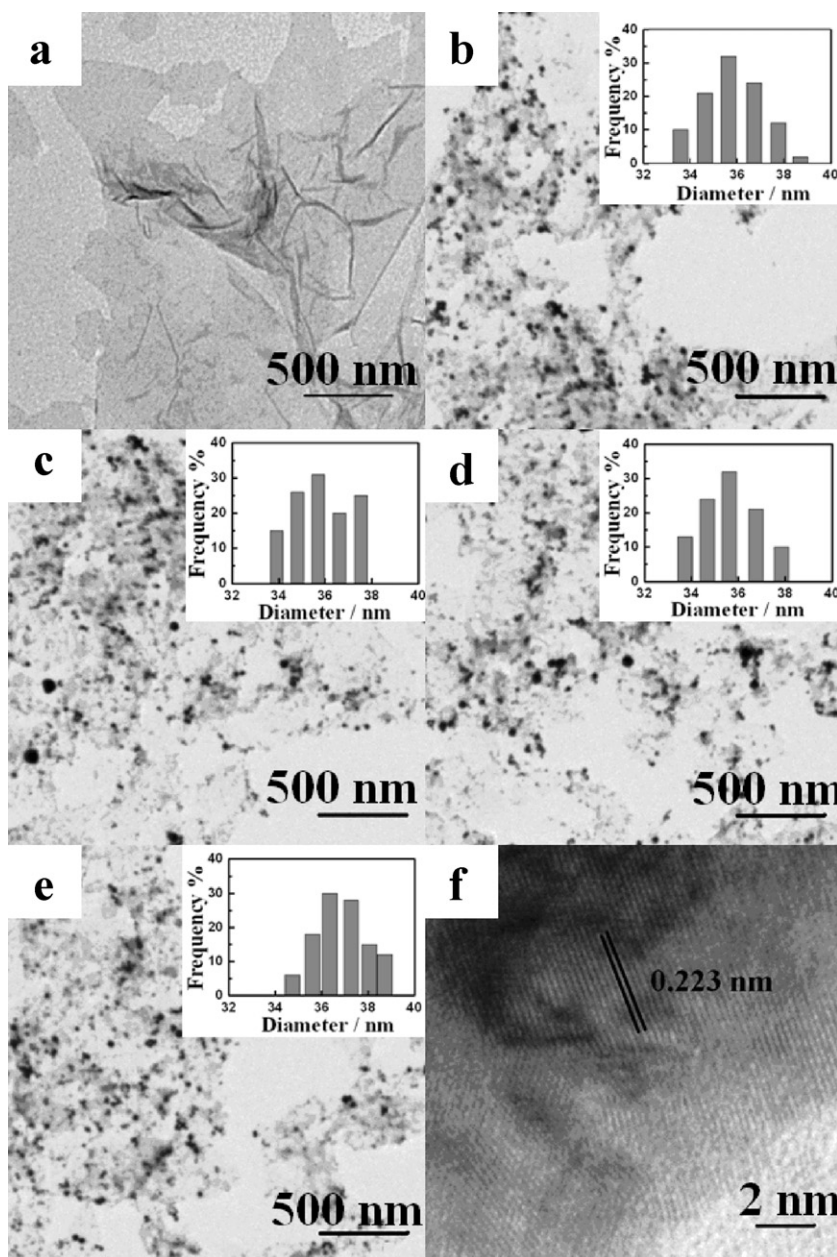

Fig. 3. TEM images of GO (a), Pt-graphene (b), and Pt-Ni-graphene nanocatalysts synthesized at $PtCl_6{}^{2-}/Ni^{2+}$ molar ratios of 1:0.5 (c), 1:1 (d), and 1:2 (e). (f) is a typical HRTEM image of a portion of a Pt-Ni-graphene nanocatalyst synthesized at a $PtCl_6{}^{2-}/Ni^{2+}$ molar ratio of 1:1. The insets of (b)–(e) show the DLS size distribution of the prepared Pt-Ni catalysts synthesized at different Pt/Ni molar ratios.
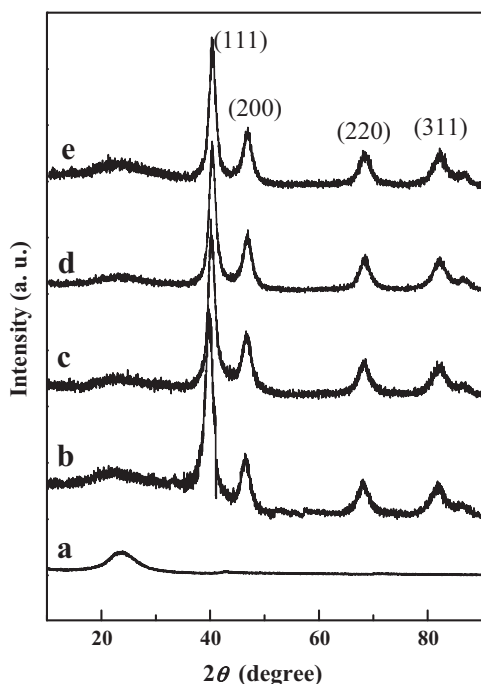
Fig. 4. The XRD patterns of graphene (a), Pt-graphene (b), and Pt-Ni-graphene nanocatalysts at Pt/Ni molar ratios of 1:0.5 (c), 1:1 (d), and 1:2 (e).

Fig. 5. The XPS spectra of Pt 4f (panel A) and Ni 2p (panel C) in the Pt-Ni-graphene nanocatalysts with a Pt/Ni molar ratio of 1:1. Panel B shows the Pt $4f_{7/2}$ peak shift in Pt-graphene (curve a) and Pt-Ni-graphene nanocatalysts with the Pt/Ni molar ratio of 1:0.5 (curve b), 1:1 (curve c), and 1:2 (curve d). The dashed line indicates the Pt $4f_{7/2}$ peak position in the Pt-graphene catalyst.

formation of an alloy with Ni. The change in the geometric or atomic configuration may affect the electronic structure of Pt [75,76], leading to an alteration in the electrocatalytic activities toward the MOR.

3.2. XPS characterization

The reactivity of the metal catalyst (e.g., Pt) can be changed substantially by alloying. For Pt-based catalysts used for MOR, Pt is usually alloyed with 3d transition metals to downshift the D-band center of the surface Pt atoms [75]. The position of the D-band center relative to the Fermi energy can be directly related to the binding energies of the reaction intermediates, such as CO. Shifting the D-band center for surface Pt is known to be accompanied by a change in the surface core-level shift in the same direction [77,78].

To examine further the surface structures of the Pt-Ni-graphene nanocatalyst, XPS measurements were performed for the nanocatalyst. Fig. 5 shows the XPS spectra of Pt 4f and Ni 2p for the Pt/Ni molar ratio of 1:1. Based on curve fitting with a mixed Gaussian–Lorentzian line shape (Fig. 5A), Pt appears to exist in various states. The 4f core-level spectrum consists of two peaks for metallic platinum at 70.6 (Pt $4f_{7/2}$) and 73.9 eV (Pt $4f_{5/2}$), with two more small peaks at approximately 71.4 and 75.1 eV that could be assigned to the Pt^{2+} species PtO and $Pt(OH)_2$ [23,79], respectively. A comparison of the relative intensities of those components (metallic Pt, PtO, and $Pt(OH)_2$) shows that Pt in the Pt-Ni-graphene nanocatalysts is predominately metallic Pt, which can provide more suitable sites for methanol decomposition than Pt(II).

An analysis of the Pt 4f peaks with respect to the molar ratio of Pt/Ni shows that the Pt 4f peaks shift to a lower binding energy with increasing Ni content in the Pt-Ni nanocatalysts (Fig. 5B), suggesting that the electronic structure of the Pt-skin layer is influenced by the Ni component in the underneath layer. The Pt 4f peak has negative shifts of approximately 0.2, 0.7, and 0.5 eV for Pt/Ni ratios of 1:0.5, 1:1, and 1:2, respectively. This negative binding energy shift may be caused by several factors, one of them is responsible for an electron donation of Ni to Pt due to the electronegativities
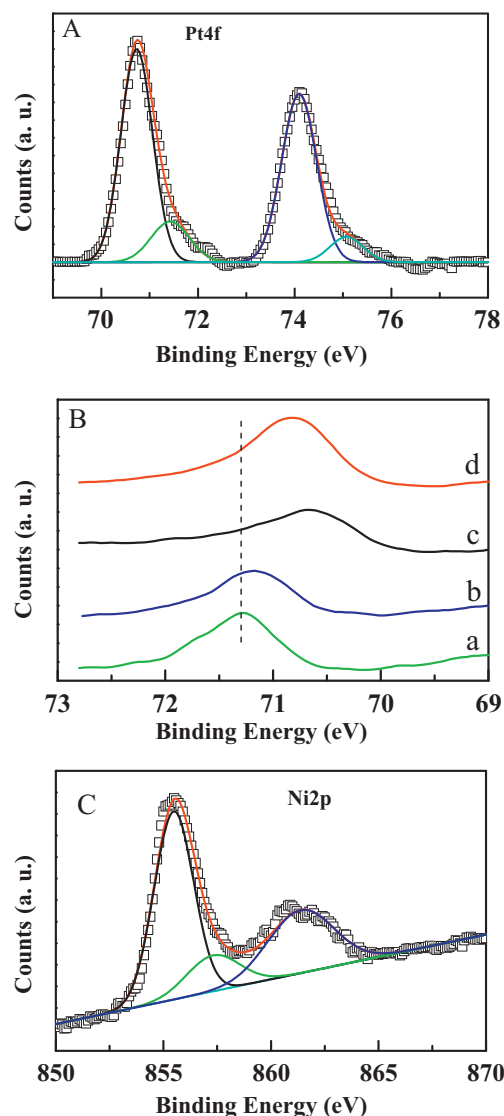
differences between Ni (1.91) and Pt (2.28). The shift in electron transfer from Ni to Pt leads to a change in the electronic characteristics of the Pt 4f, with the largest modification of the electronic characteristics of Pt occurring at a Pt/Ni molar ratio of 1:1. Such an electron transfer also lowers the density of states on the Fermi level and reduces the Pt–CO bond energy [22,80], improving the electrocatalytic activity of Pt-Ni alloys toward methanol oxidation as shown by the electrochemical measurements.

The Ni 2p core-level peaks for Pt/Ni ratio of 1:1 are depicted in Fig. 5C. In general, the Ni 2p spectrum has a complex structure with intense satellite signals of high binding energy (861.4 eV) adjacent to the main peaks, which can be attributed to multielectron excitation [81]. After these shake-up peaks are considered, the Ni 2p peaks at the binding energies of 855.6 and 857.3 eV can be ascribed to $Ni(OH)_2$ and NiOOH [68], respectively. No metallic Ni is found (it should appear at ca. 852.4 eV), suggesting that any Ni at the surface of the catalyst has been oxidized during the preparation. The surface compositions of Ni in the catalyst at the Pt/Ni molar ratios of 1:0.5, 1:1, and 1:2 are approximately 22%, 38%, and 62% (taking
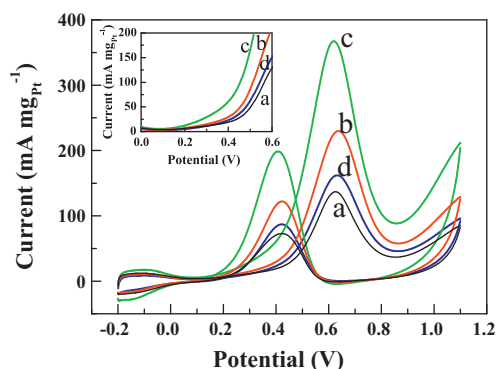
Fig. 6. The voltammetric responses of the oxidation of 0.5 M methanol at the Pt-graphene/GC (a) and the Pt-Ni-graphene/GC electrode with a Pt/Ni molar ratios of 1:0.5 (b), 1:1 (c), and 1:2 (d) in a 0.5 M H_2SO_4 solution. The current was normalized with the mass of Pt loading on the surface of the electrode. The scan rate was 50 mV s^{-1}. The inset compares the starting potential for the oxidation of methanol at the Pt-graphene/GC (a) and the Pt-Ni-graphene/GC electrode with Pt/Ni molar ratios of 1:0.5 (b), 1:1 (c), and 1:2 (d).

Fig. 7. The voltammetric responses of the oxidation of 0.5 M methanol in a 0.5 M H_2SO_4 aqueous solution at the Pt-Ni catalyst with a Pt/Ni molar ratio of 1:1 supported on graphene (a), SWNTs (b), and XC-72 carbon (c). The scan rate was 50 mV s^{-1}. The inset compares the starting potential for the oxidation of methanol at the Pt-Ni catalyst with a Pt/Ni molar ratio of 1:1 supported on graphene (a), SWNTs (b), and XC-72 carbon (c), respectively.

the sum of Pt and Ni as 100%), respectively, suggesting that Pt is an enriched metal component on the surface of the nanocatalysts, which is beneficial to enhance the catalytic activity of the catalyst.

The oxygen species (e.g., PtO, Pt(OH)$_2$, Ni(OH)$_2$, and NiOOH) that are present in the Pt-Ni nanocatalysts are surface and subsurface oxidative states and not crystalline oxidative states because no such oxides peaks are apparent in the XRD patterns of the catalyst (Fig. 4). The nickel hydroxide layer on the catalysts has some favorable properties, such as proton and electronic conductivity, and protection of the catalyst against corrosion during methanol oxidation [82,83]. This hydroxide layer on the surface of the Pt-Ni-graphene catalyst may also display catalytic activity with respect to methanol oxidation.

3.3. Electrochemical measurements

Using voltammetry, the electrocatalytic characteristics of the graphene-supported Pt-Ni nanocatalysts at the prepared Pt/Ni molar ratios were evaluated for the oxidation of methanol in an acidic solution (0.5 M H_2SO_4) as a model reaction to reveal effects of the surface composition and the electronic characteristics on the electrochemical activity of the catalyst. The electrocatalytic currents were normalized by the mass of the loading Pt on the electrode surface (Fig. 6). Well-defined anodic peaks were observed at approximately 0.64 V in the forward sweep and at 0.45 V in the reverse sweep for the Pt-graphene and Pt-Ni-graphene nanocatalysts. The Pt-Ni-graphene catalysts showed much higher catalytic activity than the Pt-graphene catalyst. The starting potential for methanol oxidation at the Pt-Ni-graphene catalyst is more negative than that at the Pt-graphene catalyst (please refer to the inset of Fig. 6). The peak current was enhanced by the increased Ni content in the Pt-Ni-graphene nanocatalysts (curves b and c) and reached its highest value at a Pt/Ni molar ratio of 1:1 (curve c). However, further increases in the Pt/Ni molar ratio (for example, 1:2) significantly decreased the anodic current (curve d).

The Ni content-dependent catalytic characteristics of the Pt-Ni-graphene nanocatalysts for MOR can be understood based on the modification of the electronic properties of Pt by Ni in the catalysts. The XPS measurements show that Ni, when alloyed with Pt, can modify the electronic structure of Pt due to the charge transfer from Ni to Pt (Fig. 5B), leading to a lower density of states at the Fermi level. The Pt-alloyed Ni can also reduce the Pt–CO bond energy and weaken the CO adsorption on Pt-Ni alloys [16,80]. Therefore, the electrocatalytic activity of the Pt-Ni catalysts is improved compared to Pt itself. Moreover, the Pt-Ni-graphene nanocatalysts exhibit the
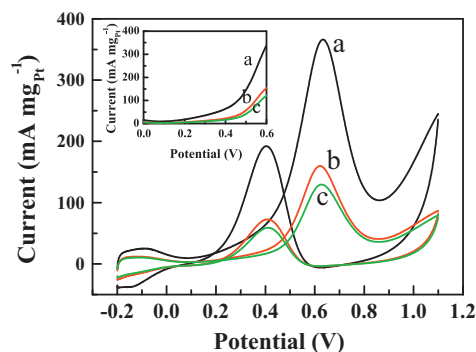
lowest binding energy at the Pt/Ni molar ratio of 1:1 (curve c in Fig. 5B), indicating that the lowest Pt–CO bond energy is reached at this composition. Therefore, the catalytic activity of the Pt-Ni-graphene catalysts reaches its highest value when the Pt/Ni molar ratio is 1:1 (Fig. 6).

The electrocatalytic features of the Pt-Ni-graphene nanocatalysts can also be understood based on the synergistic role of Pt and Ni in the catalysts. The electrochemical oxidation of methanol involves the major steps of methanol adsorption and successive dehydrogenation to intermediates (e.g., CO) and CO oxidation to the final product of CO_2 [14,15]. Platinum provides adsorption sites and activates the C–H bond cleavage of the adsorbed methanol. During this process, the Pt-CO species is formed and is strongly adsorbed onto the Pt surface, blocking the activation sites for methanol adsorption and inhibiting the oxidation of methanol. For Pt-Ni alloy catalysts, the nickel hydroxide species, which exists on the surface of the catalyst (as indicated by XPS in Fig. 5C), may offer OH species to remove the intermediate CO and reproduce the Pt activate sites for methanol adsorption [84]. Therefore, the peak current is enhanced by the increase of in the Ni content of the Pt-Ni-graphene catalyst (curves b and c in Fig. 6) and reaches its highest value at a Pt/Ni molar ratio of 1:1 (curve c). However, when the Ni content is further increased to 1:2, the surface layer of the catalyst is dominated by Ni atoms, and fewer metallic Pt atoms are available on the catalyst surface for methanol chemisorption, as shown by the XPS measurements (please refer to XPS characterization). Therefore, the Ni-dominated surface hinders methanol oxidation, even if an electronic effect still exists. This hindrance leads to a significant decrease in the oxidation current (curve d in Fig. 6).

3.4. Effects of the carbon support properties

The electrocatalytic characteristics of the Pt-Ni alloy catalyst on the MOR is significantly dependent on the structure and properties of the carbon supports, such as graphene, SWNTs, and Vulcan XC-72 carbon. To better understand the role of the different carbon supports on the electrocatalytic activity of the Pt-Ni catalyst, catalysts with a Pt/Ni molar ratio of 1:1 were prepared on the surfaces of SWNTs (denoted as Pt-Ni-SWNT) and Vulcan XC-72 carbon (denoted as Pt-Ni-XC-72C). The total metal (Pt + Ni) loading was 40 wt%. The electrocatalytic activities for the oxidation of 0.5 M methanol were studied and compared with the Pt-Ni-graphene catalyst. The voltammetric features (i.e., the positions and shapes of the oxidation peaks) of the oxidation of methanol by the Pt-Ni-XC-72C and Pt-Ni-SWNT catalysts are similar to the Pt-Ni-graphene catalyst (Fig. 7). However, the peak current
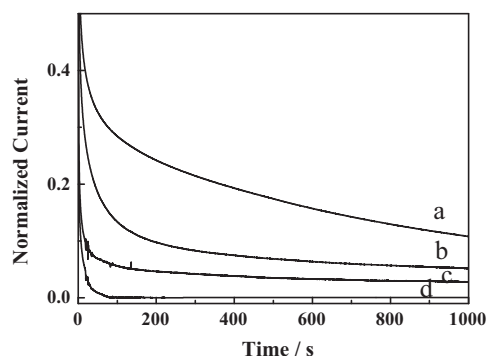
Fig. 8. A comparison of the stability of the Pt-Ni catalyst with a Pt/Ni molar ratio of 1:1 supported on graphene (a), SWNTs (b), and XC-72 carbon (c) for the electrochemical oxidation 0.5 M methanol in a 0.5 M H_2SO_4 aqueous solution under a constant potential of 0.64 V (versus SCE). The currents presented in curves (a)–(c) were normalized with the highest current obtained at the Pt-Ni-graphene, Pt-Ni-SWNT, and Pt-Ni-XC-72C catalysts, respectively. Curve (d) is the amperometric response of Pt-Ni-graphene catalyst in a 0.5 M H_2SO_4 aqueous solution without presence of methanol under a constant potential of 0.64 V. The current was normalized with the highest current obtained at the Pt-Ni-graphene catalyst in a 0.5 M H_2SO_4 solution without presence of methanol.

Fig. 9. The Raman spectra of the Pt-Ni-graphene (a), Pt-Ni-SWNT (b), and Pt-Ni-XC-72C catalysts (c).

(normalized by the mass of Pt loading on the electrode surface) obtained at the Pt-Ni-graphene catalyst (ca. 370 mA (mg Pt)$^{-1}$, curve a, Fig. 7) is much higher than the current obtained at the Pt-Ni-SWNT (ca. 160 mA (mg Pt)$^{-1}$, curve b) and Pt-Ni-XC-72C catalysts (ca. 130 mA (mg Pt)$^{-1}$, curve c). Moreover, the starting potential for methanol oxidation at the Pt-Ni-graphene catalyst is about 110 mV, which is 100 mV more negative than the potential at the Pt-Ni-SWNT or Pt-Ni-CX72C catalyst (please refer to the inset of Fig. 7), indicating that graphene has a significant role in enhancing the electrocatalytic activity of the Pt-Ni catalyst in the oxidation of methanol.

The peak current obtained at the Pt-Ni-graphene catalyst (370 mA (mg Pt)$^{-1}$, for 0.5 M methanol) is comparable with 376 and 323.6 mA (mg Pt)$^{-1}$ for the oxidation of 0.5 M methanol at the Pd-Pt catalyst [72] and the graphene/Pt-on-Pd bimetallic nanodendrite hybrids catalyst [85], respectively. However, this value is much higher than the values of 51 and 199.6 mA (mg Pt)$^{-1}$ obtained with a commercial carbon-supported platinum (Pt/XC-72 carbon, E-Tek, 60% Pt, 6 nm in diameter for Pt) [86] and Pt-graphene catalyst [87], respectively, indicating the remarkably high catalytic activity of the prepared Pt-Ni-graphene catalyst toward MOR.

The long-term stabilities of the Pt-Ni-graphene, Pt-Ni-SWNT, and Pt-Ni-XC-72C catalysts with the Pt/Ni molar ratio of 1:1 were evaluated by amperometric measurements under a constant potential of 0.64 V. The polarization currents at these catalysts decreased rapidly at the initial stage (Fig. 8), which is due to the formation of intermediate species during methanol oxidation [88]. However, the oxidation current at the Pt-Ni-graphene catalyst (curve a, Fig. 8) is still higher than the Pt-Ni-SWNT (curve b) and Pt-Ni-XC-72C catalysts (curve c) at a time of 1000 s. This finding indicates that graphene can also enhance the electrocatalytic stability of the Pt-Ni catalyst during methanol oxidation in comparison with SWNT and XC-72 carbon. These results are consistent with the voltammetric measurements (Fig. 7), suggesting that graphene has better tolerance for the intermediate species than SWNT and XC-72 carbon. Curve (d) in Fig. 7 indicates that the Pt-Ni catalyst is stable in the experimental conditions.

The oxygen-containing functional groups of SWNTs, such as the hydroxyl group, can improve the electrocatalytic characteristics of Pt-SWNT and Pd-SWNT catalysts by removing accumulated carbonaceous species (e.g., CO_{ad}) that are formed during the oxidation of methanol [89,90]. These oxygen-containing functional groups assume the role of Ru as a secondary catalyst in the case of
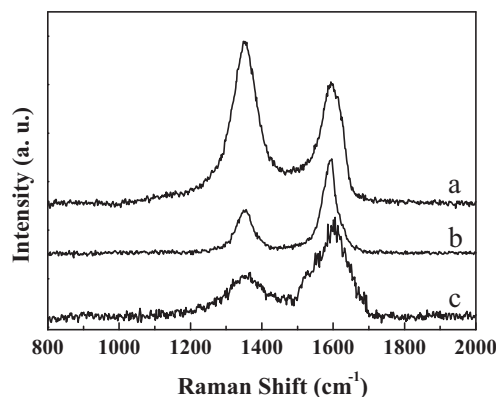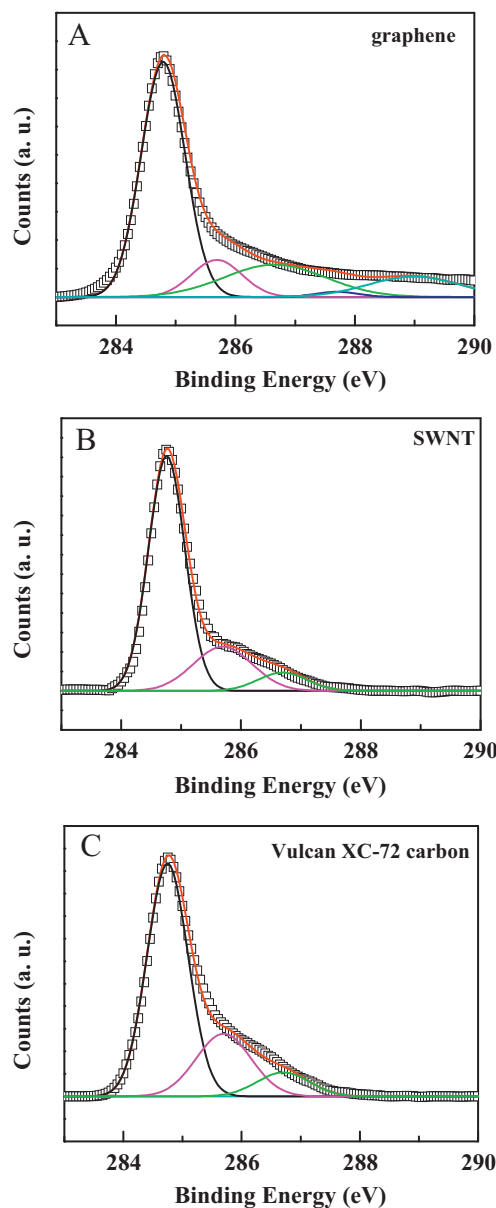

Fig. 10. The XPS spectra of the C1s and the relative curve-fitted components for the Pt-Ni-graphene (A), Pt-Ni-SWNT (B), and Pt-Ni-XC-72C catalysts (C).

Table 2
The compositions of the oxygen-containing groups on the surface of Pt-Ni-graphene, Pt-Ni-SWNT, and Pt-Ni-XC-72C catalysts with a Pt/Ni molar ratio of 1:1.

Carbon material	Component area ratio (%)				
	C–C (sp^2)	C–N (or C–C, sp^3)	C–OH	C=O	O–C=O
Graphene	59.5	10.7	18.8	1.3	9.7
SWNT	78.4	16.0	5.4	<0.1	<0.1
Vulcan XC-72 carbon	76.6	18.7	4.5	<0.1	<0.1

the Pt-Ru catalyst [91]. To understand how graphene can enhance the catalytic features of the Pt-Ni catalyst, the structures and the properties of graphene, SWNTs, and Vulcan XC-72 carbon were characterized by Raman spectroscopy and XPS.

The Raman spectra of Pt-Ni-graphene (curve a, Fig. 9), Pt-Ni-SWNT (curve b), and Pt-Ni-XC-72C catalyst (curve c) show that all of the samples exhibit two bands: the D band at approximately $1350\,cm^{-1}$ and the G band at approximately $1590\,cm^{-1}$ (Fig. 9). These peaks represent the disordered graphite and the ordered state of sp^2 carbon atoms [91], respectively. The intensity of the D band of graphene is significantly higher than SWNTs and Vulcan XC-72 carbon. This result indicates that the perfect two-dimensional graphitization of the graphene has been partially destroyed due to the reduction by hydrazine, causing the formation of the disordered structure [92]. The intensity ratio of the D peak to the G peak (I_D/I_G) can be used to estimate the amount of oxygen-containing functional groups on the surface of the carbon materials [65], although the ratio may be influenced by edges, charge puddles, ripples, or other defects [93]. The I_D/I_G ratio of graphene (1.21, curve a, Fig. 9) is much higher than those of SWNTs (0.70, curve b) and Vulcan XC-72 carbon (0.52, curve c), suggesting that more oxygen-containing functional groups are located on the surface of graphene than on SWNTs or Vulcan XC-72 carbon. These abundant functional groups on the graphene surface enhance the electrocatalytic features of the Pt-Ni-graphene catalysts, as shown in Figs. 7 and 8.

XPS was applied to study the effects of the compositions of the oxygen-containing groups on the surface of different carbon materials on the electrocatalytic characteristics of the prepared Pt-Ni catalysts. Fig. 10 shows the XPS spectra of C1s and their relative curve-fitted components for Pt-Ni-graphene (panel A), Pt-Ni-SWNT (panel B), and Pt-Ni-72C catalysts (panel C). The main peak at 284.6 eV was assigned to the sp^2-hybridized C–C. The peaks at 285.7, 286.7, 287.7, and 289.0 eV are ascribed to the sp^3 hybridized C–N or C–C (285.7 eV), C–OH (286.7 eV), C=O (287.7 eV), and O–C=O (289.0 eV), respectively [94]. By integrating the area under each peak, the compositions of the oxygen-containing groups on the carbon materials can be evaluated and are presented in Table 2. Relatively large amount of –OH, –COOH, and C=O groups are present on the surface of graphene, as compared to the SWNTs and Vulcan XC-72 carbon (Fig. 10B and C and Table 2). The number of –COOH and C=O groups on the surface of the SWNT and Vulcan XC-72 carbon is too small to be distinguished from the curve-fitted components (less than 0.1%). The number of –OH groups on the surface of graphene, SWNTs, and Vulcan XC-72 carbon decreases in the order of graphene > SWNT > Vulcan XC-72 carbon (Table 2). It has been reported that functional groups, such as –OH, can assist methanol oxidation by supplying –OH groups to the intermediates species (for example CO_{ad}), hence promoting the production of CO_2 at less positive potentials, and are responsible for improving the electrocatalytic activity of metal catalysts [57,90,95]. Therefore, the Pt-Ni-graphene nanocatalyst has greater catalytic activity than the Pt-Ni-SWNT and Pt-Ni-XC-72C catalysts. The decrease of the oxygen-containing groups on the surface of the SWNTs and Vulcan XC-72 carbon leads to the decrease in the catalytic activities.

4. Conclusions

In summary, the graphene-supported Pt-Ni alloy nanocatalysts have been prepared by one-step reduction of graphene oxide and the Ni^{2+} and $PtCl_6^{2-}$ ions. The structure, composition, and electrocatalytic activity of the nanocatalyst can be easily controlled by simply altering the molar ratio of the Pt and Ni precursors. Using voltammetry, the electrocatalytic characteristics of the nanocatalysts at the different Pt/Ni molar ratios for methanol oxidation in an acidic solution ($0.5\,M\,H_2SO_4$) were studied to evaluate effects of the structure, surface compositions, and electronic characteristics. The Pt-Ni nanocatalyst with a Pt/Ni molar ratio of 1:1 exhibited the highest electrocatalytic activity by greatly lowering the Pt utilization and enhancing the electrocatalytic stability. The results can be explained based on alterations of the electronic characteristics of the Pt 4f due to the shift in electron transfer from Ni to Pt, and the synergistic role of the Pt and nickel hydroxides existing on the surface of the catalysts. In addition, the effects of different carbon supports (i.e., graphene, single-walled carbon nanotubes, and Vulcan XC-72 carbon) on the electrocatalytic characteristics of the nanocatalysts have been investigated and explained by the Raman and X-ray photoelectron spectroscopic results. These results demonstrate that the graphene-supported Pt-Ni catalyst has the highest electrocatalytic activity among the three tested carbon materials due to abundant oxygen-containing groups on the graphene surface, which can remove the poisoned intermediates and improve the electrocatalytic activity of the catalysts.

References

[1] A.F. Shao, Z.B. Wang, Y.Y. Chu, Z.Z. Jiang, G.P. Yin, Y. Liu, Fuel Cells 10 (2010) 472–477.
[2] X.Z. Fu, Y. Liang, S.P. Chen, J.D. Lin, D.W. Liao, Catal. Commun. 10 (2009) 1893–1897.
[3] K.L. Nagashree, N.H. Raviraj, M.F. Ahmed, Electrochim. Acta 55 (2010) 2629–2635.
[4] L. Wang, Y. Nemoto, Y. Yamauchi, J. Am. Chem. Soc. 133 (2011) 9674–9677.
[5] Z.F. Liu, G.S. Jackson, B.W. Eichhorn, Angew. Chem. Int. Ed. 49 (2010) 3173–3176.
[6] J.B. Wu, J.L. Zhang, Z.M. Peng, S.C. Yang, F.T. Wagner, H. Yang, J. Am. Chem. Soc. 132 (2010) 4984–4985.
[7] D. Xu, S. Bliznakov, Z.P. Liu, J.Y. Fang, N. Dimitrov, Angew. Chem. Int. Ed. 49 (2010) 1282–1285.
[8] J. Zhang, H.Z. Yang, J.Y. Fang, S.Z. Zou, Nano Lett. 10 (2010) 638–644.
[9] Y.J. Kang, C.B. Murray, J. Am. Chem. Soc. 132 (2010) 7568–7569.

[10] J. Kim, Y. Lee, S.H. Sun, J. Am. Chem. Soc. 132 (2010) 4996–4997.
[11] S. Park, T.D. Chung, H.C. Kim, Anal. Chem. 75 (2003) 3046–3049.
[12] J.H. Yuan, K. Wang, X.H. Xia, Adv. Funct. Mater. 15 (2005) 803–809.
[13] Q. Shen, L. Jiang, H. Zhang, Q. Min, W. Hou, J.J. Zhu, J. Phys. Chem. C 112 (2008) 16385–16392.
[14] J.S. Spendelow, J.D. Goodpaster, P.J.A. Kenis, A. Wieckowski, Langmuir 22 (2006) 10457–10464.
[15] J.S. Spendelow, G.Q. Lu, P.J.A. Kenis, A. Wieckowski, J. Electroanal. Chem. 568 (2004) 215–224.
[16] Q. Jiang, L. Jiang, H. Hou, J. Qi, S. Wang, G. Sun, J. Phys. Chem. C 114 (2010) 19714–19722.
[17] R. Loukrakpam, J. Luo, T. He, Y. Chen, Z. Xu, P.N. Njoki, B.N. Wanjala, B. Fang, D. Mott, J. Yin, J. Klar, B. Powell, C.J. Zhong, J. Phys. Chem. C 115 (2011) 1682–1694.
[18] I. Matanović, F.H. Garzon, N.J. Henson, J. Phys. Chem. C 115 (2011) 10640–10650.
[19] Z.B. Wang, C.R. Zhao, P.F. Shi, Y.S. Yang, Z.B. Yu, W.K. Wang, G.P. Yin, J. Phys. Chem. C 114 (2010) 672–677.
[20] S.J. Hwang, S.J. Yoo, S. Jang, T.H. Lim, S.A. Hong, S.K. Kim, J. Phys. Chem. C 115 (2011) 2483–2488.
[21] T.Y. Jeon, S.J. Yoo, Y.H. Cho, K.S. Lee, H. Kang, Y.E. Sung, J. Phys. Chem. C 113 (2009) 19732–19739.
[22] K.W. Park, J.H. Choi, Y.E. Sung, J. Phys. Chem. B 107 (2003) 5851–5856.
[23] K. Zhang, Q. Yue, G. Chen, Y. Zhai, L. Wang, H. Wang, J. Zhao, J. Liu, J. Jia, H. Li, J. Phys. Chem. C 115 (2011) 379–389.
[24] R. Mu, Q. Fu, H. Xu, H. Zhang, Y. Huang, Z. Jiang, S. Zhang, D. Tan, X. Bao, J. Am. Chem. Soc. 133 (2011) 1978–1986.
[25] K.R. Lee, M.K. Jeon, S.I. Woo, Appl. Catal. B: Environ. 91 (2009) 428–433.
[26] E. Antolini, J.R.C. Salgado, E.R. Gonzalez, Appl. Catal. B: Environ. 63 (2006) 137–149.
[27] B.N. Wanjala, J. Luo, R. Loukrakpam, D. Mott, P.N. Njoki, B. Fang, M. Engelhard, H.R. Naslund, J.K. Wu, L. Wang, O. Malis, C.J. Zhong, Chem. Mater. 22 (2010) 4282–4294.
[28] F.H.B. Lima, E.A. Ticianelli, Electrochim. Acta 49 (2004) 4091–4099.
[29] T. He, E. Kreidler, L.F. Xiong, J. Power Sources 165 (2007) 87–91.
[30] T. He, E. Kreidler, L.F. Xiong, J. Luo, C.J. Zhong, J. Electrochem. Soc. 153 (2006) A1637–A1643.
[31] S. Chen, W.C. Sheng, N. Yabuuchi, P.J. Ferreira, L.F. Allard, Y. Shao-Horn, J. Phys. Chem. C 113 (2009) 1109–1125.
[32] S. Koh, M.F. Toney, P. Strasser, Electrochim. Acta 52 (2007) 2765–2774.
[33] Z.F. Liu, J.E. Hu, Q. Wang, K. Gaskell, A.I. Frenkel, G.S. Jackson, B. Eichhorn, J. Am. Chem. Soc. 131 (2009) 6924–6925.
[34] K.W. Park, J.H. Choi, B.K. Kwon, S.A. Lee, Y.E. Sung, J. Phys. Chem. B 106 (2002) 1869–1877.
[35] M.V. Martínez-Huerta, S. Rojas, J.L. Gómez de-la-Fuente, P. Terreros, M.A. Peña, J.L.G. Fierro, Appl. Catal. B: Environ. 69 (2009) 75–84.
[36] Z.Q. Tian, S.P. Jiang, Y.M. Liang, P.K. Shen, J. Phys. Chem. B 110 (2006) 5343–5350.
[37] H.D. Du, B.H. Li, F.Y. Kang, R.W. Fu, Y.Q. Zeng, Carbon 45 (2007) 429–435.
[38] S. Kim, M.H. Cho, J.R. Lee, S.J. Park, J. Power Sources 159 (2006) 46–48.
[39] D.A. Konopka, M. Li, K. Artyushkova, N. Marinkovic, K. Sasaki, R. Adzic, T.L. Ward, P. Atanassov, J. Phys. Chem. C 115 (2011) 3043–3056.
[40] B.Z. Fang, M. Kim, J.S. Yu, Appl. Catal. B: Environ. 84 (2008) 100–105.
[41] Y.Y. Shao, G.P. Yin, Y.Z. Gao, P.F. Shi, J. Electrochem. Soc. 153 (2006) A1093–A1097.
[42] I.S. Park, K.W. Park, J.H. Choi, C.R. Park, Y.E. Sung, Carbon 45 (2007) 28–33.
[43] H. Yang, C. Coutanceau, J.M. Léger, N. Alonso-Vante, C. Lamy, J. Electroanal. Chem. 576 (2005) 305–313.
[44] J. Lobato, P. Cañizares, M.A. Rodrigo, J.J. Linares, R. López-Vizcaíno, Energy Fuels 22 (2008) 3335–3345.
[45] C.T. Hsieh, J.Y. Lin, J. Power Sources 188 (2009) 347–352.
[46] J. Lobato, P. Cañizares, D. Ubeda, F.J. Pinar, M.A. Rodrigo, Appl. Catal. B: Environ. 106 (2011) 174–180.
[47] S.St. John, I. Dutta, A.P. Angelopoulos, Langmuir 27 (2011) 5781–5791.
[48] J. Qi, L. Jiang, S. Wang, G. Sun, Appl. Catal. B: Environ. 107 (2011) 95–103.
[49] K.Y. Chan, J. Ding, J.W. Ren, S.A. Cheng, K.Y. Tsang, J. Mater. Chem. 14 (2004) 505–516.
[50] H. Yang, F. Li, C. Shan, D. Han, Q. Zhang, L. Niu, A. Ivaska, J. Mater. Chem. 19 (2009) 4632–4638.
[51] R. Kou, Y. Shao, D. Mei, Z. Nie, D. Wang, C. Wang, V.V. Viswanathan, S. Park, I.A. Aksay, Y. Lin, Y. Wang, J. Liu, J. Am. Chem. Soc. 133 (2011) 2541–2547.
[52] F. Yang, Y. Liu, L. Gao, J. Sun, J. Phys. Chem. C 114 (2010) 22085–22091.
[53] X.M. Wu, Y.J. Hu, J. Jin, N.L. Zhou, P. Wu, H. Zhang, C.X. Cai, Anal. Chem. 82 (2010) 3588–3596.
[54] P. Wu, Q. Shao, Y.J. Hu, J. Jin, Y.J. Yin, H. Zhang, C.X. Cai, Electrochim. Acta 55 (2010) 8606–8614.
[55] A. Guha, W. Lu, T.A. Zawodzinski Jr., D.A. Schiraldi, Carbon 45 (2007) 1506–1517.
[56] C.C. Chen, C.F. Chen, C.M. Chen, F.T. Chuang, Electrochem. Commun. 9 (2007) 159–163.
[57] A. Halder, S. Sharma, M.S. Hegde, N. Ravishankar, J. Phys. Chem. C 113 (2009) 1466–14763.
[58] Y.J. Hu, H. Zhang, P. Wu, H. Zhang, B. Zhou, C.X. Cai, Phys. Chem. Chem. Phys. 13 (2011) 4083–4094.
[59] Y.J. Hu, J. Jin, P. Wu, H. Zhang, C.X. Cai, Electrochim. Acta 56 (2010) 491–500.
[60] H. Zhang, X.Q. Xu, P. Gu, C.Y. Li, P. Wu, C.X. Cai, Electrochim. Acta 56 (2011) 7064–7070.
[61] N. Shang, P. Papakonstantinou, P. Wang, S.R.P. Silva, J. Phys. Chem. C 114 (2010) 15837–15841.
[62] Q. Yue, K. Zhang, X. Chen, L. Wang, J. Zhao, J. Liu, J. Jia, Chem. Commun. 46 (2010) 3369–3371.
[63] W.S. Hummers, R.E. Offeman, J. Am. Chem. Soc. 80 (1958) 1339.
[64] J.L. Elechiguerra, J.L. Burt, J.R. Morones, A. Camacho-Bragado, X. Gao, H.H. Lara, M.J. Yacaman, J. Nanobiotechnol. 3 (2005) 6.
[65] D. Luo, G. Zhang, J. Liu, X. Sun, J. Phys. Chem. C 115 (2011) 11327–11335.
[66] C. Shan, H. Yang, D. Han, Q. Zhang, A. Ivaska, L. Niu, Biosens. Bioelectron. 25 (2010) 1070–1074.
[67] H. Liu, J. Gao, M. Xue, N. Zhu, M. Zhang, T. Cao, Langmuir 25 (2009) 12006–12010.
[68] T.C. Deivaraj, W. Chen, J.Y. Lee, J. Mater. Chem. 13 (2003) 2555–2560.
[69] F. Li, J. Chai, H. Yang, D. Han, L. Niu, Talanta 81 (2010) 1063–1068.
[70] D. Long, W. Li, L. Ling, J. Miyawaki, I. Mochida, S.H. Yoon, Langmuir 26 (2010) 16096–16102.
[71] N.G. Shang, P. Papakonstantinou, M. Mcmullan, M. Chu, A. Stamboulis, A. Potenza, S.S. Dhesi, H. Marchetto, Adv. Funct. Mater. 18 (2008) 3506–3514.
[72] H. Zhang, Y.J. Yin, Y.J. Hu, C.Y. Li, P. Wu, S.H. Wei, C.X. Cai, J. Phys. Chem. C 114 (2010) 11861–11867.
[73] L. Tang, Y. Wang, Y. Li, H. Feng, J. Lu, J. Li, Adv. Funct. Mater. 19 (2009) 2782–2789.
[74] H. Yang, W. Vogel, C. Lamy, N. Alonso-Vante, J. Phys. Chem. B 108 (2004) 11024–11034.
[75] J.R. Kitchin, J.K. Nørskov, M.A. Barteau, G. Chen, J. Chem. Phys. 120 (2004) 10240–10246.
[76] V.R. Stamenkovic, B. Fowler, B.S. Mun, G. Wang, P.N. Ross, C.A. Lucas, N.M. Markovic, Science 315 (2007) 493–497.
[77] B. Hammer, J.K. Nørskov, Adv. Catal. 45 (2000) 71–129.
[78] M.V. Ganduglia-Pirovano, V. Natoli, M.H. Cohen, J. Kudrnovsky, I. Turek, Phys. Rev. B 54 (1996) 8892–8898.
[79] F. Liu, J.Y. Lee, W.J. Zhou, Small 2 (2006) 121–128.
[80] Y. Ishikawa, M.S. Liao, C.R. Cabrera, Surf. Sci. 463 (2000) 66–80.
[81] T.C. Shobha, L. Aravina, P. Bera, L.G. Devi, S.M. Mayanna, Mater. Chem. Phys. 80 (2003) 656–661.
[82] A.A. El-Shafei, J. Electroanal. Chem. 471 (1999) 89–95.
[83] A. Kowal, S.N. Port, R.J. Nichols, Catal. Today 38 (1997) 483–492.
[84] P.K. Shen, C.W. Xu, R. Zeng, Y.L. Liu, Electrochem. Solid-State Lett. 9 (2006) A39–A42.
[85] S. Guo, S. Dong, E. Wang, ACS Nano 4 (2010) 547–555.
[86] X.W. Teng, X.Y. Liang, S. Maksimuk, H. Yang, Small 2 (2006) 249–253.
[87] Y. Li, L. Tang, J. Li, Electrochem. Commun. 11 (2009) 846–849.
[88] S. Papadimitriou, S. Armyanov, E. Valova, A. Hubin, O. Steenhaut, E. Pavlidou, G. Kokkinidis, S. Sotiropoulos, J. Phys. Chem. C 114 (2010) 5217–5223.
[89] J. Chen, M. Wang, B. Liu, Z. Fan, K. Cui, Y. Kuang, J. Phys. Chem. B 110 (2006) 11775–11779.
[90] L. Meng, J. Jin, G.X. Yang, T.H. Lu, H. Zhang, C.X. Cai, Anal. Chem. 81 (2009) 7271–7280.
[91] R.V. Hull, L. Li, Y. Xing, C.C. Chusuei, Chem. Mater. 18 (2006) 1780–1788.
[92] J. Zhang, H. Yang, G. Shen, P. Cheng, J. Zhang, S. Guo, Chem. Commun. 46 (2010) 1112–1114.
[93] C.N.R. Rao, A.K. Sood, K.S. Subrahmanyam, A. Govindaraj, Angew. Chem. Int. Ed. 48 (2009) 7752–7777.
[94] C. Shan, H. Yang, J. Song, D. Han, A. Ivaska, L. Niu, Anal. Chem. 81 (2009) 2378–2382.
[95] P. Hernández-Fernández, S. Baranton, S. Rojas, P. Ocón, J.-M. Léger, J.L.G. Fierro, Langmuir 27 (2011) 9621–9629.